Plasmon-resonant gold nanorods provide spectroscopic OCT contrast in excised human breast tumors

Amy L. Oldenburg[a], Matthew N. Hansen[b], Alexander Wei[b], Stephen A. Boppart*[a]

[a]Beckman Institute for Advanced Science and Technology, Department of Electrical and Computer Engineering, University of Illinois at Urbana-Champaign, 405 N. Mathews Ave., Urbana, IL 61801
[b]Department of Chemistry, Purdue University, 560 Oval Dr., West Lafayette, IN 47907

ABSTRACT

Plasmon-resonant gold nanorods have been demonstrated recently as contrast agents for optical coherence tomography (OCT). To evaluate their ability to produce contrast in a structurally heterogeneous environment, nanorods were injected at discrete locations into an excised sample of human breast invasive ductal carcinoma. The distribution of nanorods within the tissue was revealed using spectroscopic OCT imaging techniques, by analyzing the evolution of the backscattered light spectrum over tissue depth. We compare a variety of signal processing methods including spatial averaging and least-squares fitting to the *a priori* extinction spectrum of the nanorods, with the goal of optimizing the detection sensitivity to the nanorods in these tissues. Because nanorods can be conjugated with proteins specific to biomolecular targets, they may potentially be used with these imaging methods to provide molecular contrast in human tissues.

Keywords: Plasmon-resonance, nanorods, optical coherence tomography, contrast agents, spectroscopic optical coherence tomography

*boppart@uiuc.edu; phone 1 217 244-7479; http://biophotonics.uiuc.edu/

1. INTRODUCTION

Optical coherence tomography (OCT) is an emerging biomedical imaging modality which provides micrometer-scale resolution depth-resolved images typically a few millimeters into biological tissues [1]. However, as it is a coherence imaging method, it is insensitive to the usual array of optical fluorescent and bioluminescent imaging probes. Therefore, new methods to generate optical contrast in OCT must be developed. Currently several promising methods are being investigated, including a pump-probe spectroscopic method for measuring endogenous chromophores [2], magnetic nanoparticles modulated by an external magnetic field gradient [3], and plasmon-resonant nanoshells [4], nanocages [5], and nanorods [6] which exhibit resonant absorption or scattering within the laser wavelength band.

As plasmon-resonant nanoparticles exhibit sharp extinction spectra, they are particularly inducive to spectroscopic OCT detection techniques [7], as demonstrated for sensing NIR absorbing dyes [8] and plasmon-resonant gold nanocages [5]. Given *a priori* information about the tissue and contrast agents' extinction spectra, it is possible to quantitate their relative concentrations within an image using a least-squares analysis [9]. However, this analysis requires that the spatial and spectral image responses are separable. In practice, the transfer function of the optical system imparts a wavelength-, depth-, and surface position-dependent response that cannot easily be unmixed.

2. SIGNAL THEORY

The ability to provide simultaneous spectral, spatial, and subsequently nanorod-contrasted OCT imaging is a high-dimensionality problem that requires careful attention to avoid producing an unwanted bias into the signals, particularly when trying to sense small concentrations of nanorods against a large optical tissue scattering background. Let us define the spectral response $S(x,z,\lambda)$ in terms of the lateral position x, depth position z, and

wavelength λ, where S is the OCT signal amplitude associated with a specific wavelength component. It has been shown that accurate estimation of S requires a reference measurement taken with the sample arm of the interferometer blocked (allowing only the reference arm light to propagate toward the detector), and that it is also necessary to spatially average over multiple resolution (coherence) volumes to avoid confounding speckle noise [10]. We use the expression given in [10] which correctly accounts for these factors and avoids the problem of over-estimation of S at the edges of the spectrum. However, knowing S is only a starting point for extracting the nanorod spatial distribution, as will be detailed in the rest of this section.

2.1 Statement of the problem

We want to map the distribution of nanorods $\rho_{n,i}(x,z)$ within a tissue sample based on the spectroscopic OCT signal. The spectroscopic response S_i for a B-mode OCT image i within a group of images of the same tissue type can be written (showing explicitly all the parameter dependencies):

$$S_i\left(x,z,\lambda; z_{s,i}(x)\right)= f\left(z, z_{s,i}(x),\lambda\right)\sqrt{\rho_{s,i}(x,z)\varepsilon_{b,s}(\lambda)}\exp\left\{-\varepsilon_{t,s}(\lambda)\int_{z_{s,i}(x)}^{z}\rho_{s,i}(x,z')dz' - \varepsilon_{t,n}(\lambda)\int_{z_{s,i}(x)}^{z}\rho_{n,i}(x,z')dz'\right\} \quad (1)$$

where the parameters depending on the specific image i are:

- $z_{s,i}(x)$ is the axial position of the sample top surface

- $\rho_{s,i}(x,z)$ is the concentration distribution of endogenous scatterers and absorbers in the sample

- $\rho_{n,i}(x,z)$ is the concentration distribution of the nanorods in the sample

and the functions that are common across the group of B-mode images of the same tissue type are:

- $\varepsilon_{b,s}(\lambda)$ is the endogenous molar backscattering coefficient of the sample (without nanorods)

- $\varepsilon_{t,s}(\lambda)$ is the endogenous molar extinction coefficient of the sample (without nanorods)

- $\varepsilon_{t,n}(\lambda)$ is the molar extinction coefficient of the nanorods

- $f(z,z_{s,i}(x),\lambda)$ is the hardware transfer function accounting for chromatic aberration in the lens, camera, *etc*.

This treatment so far uses several assumptions. The nanorods must be in the a concentration regime where their extinction coefficient is linear with respect to concentration; this appears to be experimentally true in our case up to the highest concentrations we measured, which gave extinction coefficients of ~35/cm. We have neglected the contribution of the nanorods to the backscattering signal in front of the exponential because our nanorods are sufficiently small (15×45 nm) so that they are dominated by optical absorption [6]. Thus, the nanorod-specific spectroscopic response observed in S is primarily due to reduced backscattering observed as the light is spectrally attenuated by the nanorods over depth. As written, (1) also requires the tissues to lie in the linear concentration regime, however, as long as the ratio of the extinction to backscattering coefficients for the tissue remain constant, there should be no adverse effect on the estimation of $\rho_{n,i}(x,z)$ even if the estimation of $\rho_{s,i}(x,z)$ is not physically accurate.

The hardware parameter $f(z,z_{s,i}(x),\lambda)$ requires further discussion. Due to the extremely fine tolerances required to align the angularly-dispersed light beam onto the line camera in the spectrometer, the modulation transfer function varies across the pixels of the camera, and thus, since pixel number is correlated with λ and spatial modulation is proportional to z, this gives rise to a significant depth-dependent spectral modification. Tracking of the tissue top surface $z_{s,i}(x)$ is also necessary because for our extremely broadband system the lens imparts a significant depth-dependent chromatic aberration. The aberration depends on the position of the focus depth position within the sample, and since the sample is usually water-based (refractive index $n = 1.34$ or higher), this focus position changes significantly (a function of n^2z_s) as the top surface moves axially. It is possible to flatten the refractive surface using a coverslip and appropriate index-matching fluid, however, in OCT a surface aligned exactly normal to the light beam will cause a large reflection that saturates the detector. It is possible that for catheter-based or other immersed imaging applications this issue will not be a problem. For our system, we found in practice that none of these 3 parameters can be reduced or decoupled without detriment to the imaging quality. Thus, it is necessary to construct a 3-dimensional database from the *a priori* images (which will be discussed in the following subsection).

We also note that, in our system, the light beam is not scanned across the imaging lens but rather the tissue sample is mounted on its own stage for lateral scanning. This is an important point as scanning across the lens would further induce a dimensionality of x to f due to off-axis chromatic aberrations.

2.2 *A priori* data

In order to solve for $\rho_{n,i}(x,z)$, it is helpful to acquire images of the tissue medium m before introduction of the nanorods, or alternately of an optically similar medium, thus providing the following *a priori* spectral response:

$$S_m\left(x,z,\lambda;z_{s,m}(x)\right)=f\left(z,z_{s,m}(x),\lambda\right)\sqrt{\rho_{s,m}(x,z)\varepsilon_{b,s}(\lambda)}\exp\left\{-\varepsilon_{t,s}(\lambda)\int_{z_{s,m}(x)}^{z}\rho_{s,m}(x,z')dz'\right\}.\tag{2}$$

Then we can build an *a priori* database by appropriate averaging over the columns x and images m as follows:

$$S_{a\ priori}(z,z_s,\lambda)=\left\langle S_m\left(x,z,\lambda;z_{s,m}(x)\right)\right\rangle_{x,m}\quad for\quad x\quad with\quad same\quad z_s(x)\tag{3}$$

by averaging columns with similar values for $z_s(x)$ together over multiple images m. $z_s(x)$ can be found automatically by surface recognition algorithms. We computed $z_s(x)$ by stepping downward from the top of a column, finding the first pixel value above a threshold, and computing the position of the half-maximum intensity point in this region. However, manual oversight to correct for falsely identified surfaces was still necessary. Once this averaging is performed, we can correct for the many parameter dependencies in the hardware function f for an image of nanorod-laden tissue S_i by normalizing against the *a priori*:

$$\frac{S_i(x,z,\lambda)}{S_{a\ priori}(z,z_s(x),\lambda)}=\sqrt{\frac{\rho_{s,i}(x,z)}{\overline{\rho_s}}}\exp\left\{-\varepsilon_{t,s}(\lambda)\left[\int_{z_{s,i}(x)}^{z}\rho_{s,i}(x,z')dz'-\overline{\rho_s}\cdot\left(z-z_{s,i}(x)\right)\right]-\varepsilon_{t,n}(\lambda)\int_{z_{s,i}(x)}^{z}\rho_{n,i}(x,z')dz'\right\}\tag{4}$$

where $\overline{\rho_s}$ is essentially an average sample scatterer density from the *a priori* images. It helps to simplify our thinking by writing the fluctuating sample density in term of this average:

$$\rho_{s,i}(x,z)=\overline{\rho_s}\left(1+\delta_i(x,z)\right)\tag{5}$$

where δ is a unitless function that maps the fractional change in the sample i scatterer density from the average value (a function to track how homogeneous the sample is). If a sufficiently large spatial window is taken, δ will spatially average to zero. The window size needed depends on the length scale of the inhomogeneity in the tissue. Thus we can assume sufficient averaging such that δ is small with respect to 1, and by Taylor expansion about δ and applying the natural log, we derive the following expression:

$$-\ln\left(\frac{S_i}{S_{a\ priori}}\right)\approx-\frac{1}{2}\delta_i(x,z)+\varepsilon_{t,s}(\lambda)\overline{\rho_s}\int_{z_{s,i}(x)}^{z}\delta_i(x,z')dz'+\varepsilon_{t,n}(\lambda)\int_{z_{s,i}(x)}^{z}\rho_{n,i}(x,z')dz'\tag{6}$$

and by partial differentiation with respect to z:

$$-\frac{\partial}{\partial z}\ln\left(\frac{S_i}{S_{a\ priori}}\right)\approx-\frac{1}{2}\frac{\partial\delta_i(x,z)}{\partial z}+\varepsilon_{t,s}(\lambda)\overline{\rho_s}\delta_i(x,z)+\varepsilon_{t,n}(\lambda)\rho_{n,i}(x,z).\tag{7}$$

Using Eq. (6), we can solve for the integrated concentration of the nanorods from the surface z_s down to the imaging point z, then divide by $z-z_s$ to get a cumulative average of ρ_n. We'll denote this class of estimation methods based on the cumulative response with an "A". Using Eq. (7), we can directly resolve the z-dependent ρ_n using the derivative, which we'll denote with a "B". In practice, computation of the derivative can be extremely noise-prone, as we will see below.

2.3 Solutions for the nanorod spatial distribution

There are various ways in which the residual term δ may be handled and also in which the *a priori* spectra of the nanorods may be incorporated into the solution. Here we will propose 3 different methods which get progressively more sophisticated, each with A and B versions.

Method 1.A

Assume δ averages to zero over a voxel of interest, and quantify the residual, cumulative extinction coefficient using Eq. (6):

$$-\ln\left(\frac{S_i}{S_{a\ priori}}\right) = \varepsilon_{t,n}(\lambda)\langle\rho_{n,i}(x,z')\rangle_{z'=z_s\ldots z}\cdot(z-z_s)$$

$$\langle\mu_{t,n}(x,z,\lambda)\rangle_{z_s\ldots z} = \varepsilon_{t,n}(\lambda)\langle\rho_{n,i}(x,z)\rangle_{z_s\ldots z} = \frac{-\ln\left(\frac{S_n}{S_{a\ priori}}\right)}{(z-z_s)} \qquad (8)$$

We can then display the nanorod-specific extinction coefficient $\mu_{t,n}$ similarly to other SOCT data parameters [7] using the HSV (hue-saturation-value) colormap, where hue is assigned to the wavelength centroid of $\mu_{t,n}$, saturation is assigned to the mean amplitude of $\mu_{t,n}$ across the entire spectrum, and value is assigned to the OCT structural image data (to allow the viewer to co-localize the spectral information with the tissue structure). In this way, nanorods with absorption peaks tuned to one side of the OCT light spectrum will show a definite spectral shift indicative of their presence.

Method 1.B

Similar to method 1.A, now we use Eq. (7) and assume the derivative of δ averages to zero. Then we can axially resolve the residual extinction $\mu_{t,n}$ using expression:

$$-\frac{\partial}{\partial z}\ln\left(\frac{S_i}{S_{a\ priori}}\right) = \varepsilon_{t,n}(\lambda)\rho_{n,i}(x,z) = \mu_{t,n}(x,z,\lambda) \qquad (9)$$

which can then be displayed assigning HSV channels the same way as in Method 1.A. Using the Euler approximation, one can compute the derivative in a voxel centered at z by taking the difference between the voxel value at $z+\Delta z$ with the one at $z-\Delta z$ and dividing by $2\Delta z$.

Method 2.A

While the above methods give a qualitative picture of the spectral centroid shift in the residual extinction $\mu_{t,n}$, a more quantitative estimation of $\rho_{n,i}(x,z)$ can be performed as follows. Assume δ averages to zero and evaluate the cumulative ρ_n after averaging over λ:

$$\langle\rho_{n,i}(x,z)\rangle_{z_s\ldots z} = \left\langle\frac{-\ln\left(\frac{S_i}{S_{a\ priori}}\right)}{(z-z_s)\cdot\varepsilon_{t,n}(\lambda)}\right\rangle_{\lambda} \qquad (10)$$

In this case we are essentially fitting the spectral response to the *a priori* extinction spectrum of the nanorods (*e.g.*, from a spectrophotometer). This provides a numerical estimate for the concentration of the nanorods as a fraction of the concentration used in the spectrophotometer calibration measurement. This number should be positive but could become negative due to noise. To display this type of data we used an RGB (red-green-blue) colormap where the OCT structural data was assigned to the red, positive ρ_n values to the green, and negative ρ_n values to the blue channel intensity.

Method 2.B

Similar to method 2.A, we can now solve for an axially-resolved ρ_n by the following:

$$\left\langle \rho_{n,i}(x,z) \right\rangle = \left\langle \frac{-\dfrac{\partial}{\partial z} \ln\left(\dfrac{S_i}{S_{a\ priori}}\right)}{\varepsilon_{t,n}(\lambda)} \right\rangle_\lambda \tag{11}$$

where the derivative is computed as in method 1.B, and where the OCT structural and ρ_n values are assigned to a red-green-blue colormap as in method 2.A.

Method 3.A

Rather than assuming δ is negligible when averaged over the spatial voxel, we can keep the first-order term of the Taylor expansion, which is a λ-independent offset as follows:

$$-\ln\left(\frac{S_i}{S_{a\ priori}}\right) \approx -\frac{1}{2}\delta_i(x,z) + \varepsilon_{t,n}(\lambda) \int_{z_{s,i}(x)}^{z} \rho_{n,i}(x,z')dz' \tag{12}$$

which has the form of:

$$M(\lambda) = C + \varepsilon(\lambda)\rho \cdot (z - z_s) \tag{13}$$

and which has the least-squares solution:

$$\frac{\partial}{\partial \lambda}\left[M(\lambda) - C - \varepsilon(\lambda)\rho \cdot (z - z_s)\right] = 0 . \tag{14}$$

Thus, for the cumulative response from z_s to z we get:

$$\left\langle \rho_{n,i}(x,z) \right\rangle_{z_s \ldots z} = \left\langle \frac{\dfrac{\partial M(\lambda)}{\partial \lambda}}{(z - z_s) \cdot \dfrac{\partial \varepsilon(\lambda)}{\partial \lambda}} \right\rangle_\lambda = \left\langle \frac{\dfrac{\partial}{\partial \lambda}\left[-\ln\left(\dfrac{S_i}{S_{a\ priori}}\right)\right]}{(z - z_s) \cdot \dfrac{\partial \varepsilon_{t,n}(\lambda)}{\partial \lambda}} \right\rangle_\lambda . \tag{15}$$

Method 3.B

Subsequently we can write an expression using the same reasoning as in method 3.A, except now resolving ρ_n axially using Eq. (7):

$$\left\langle \rho_{n,i}(x,z) \right\rangle = \left\langle \frac{\dfrac{\partial M(\lambda)}{\partial \lambda}}{\dfrac{\partial \varepsilon(\lambda)}{\partial \lambda}} \right\rangle_\lambda = \left\langle \frac{\dfrac{\partial^2}{\partial \lambda \partial z}\left[-\ln\left(\dfrac{S_i}{S_{a\ priori}}\right)\right]}{\dfrac{\partial \varepsilon_{t,n}(\lambda)}{\partial \lambda}} \right\rangle_\lambda . \tag{16}$$

Note that, while this is the most sophisticated technique as it provides depth-resolution, accounts for the *a priori* nanorods spectrum, and places less restrictions on the size of the tissue spatial inhomogeneity δ, it requires two partial differentiations be performed on the spectral response data.

3. EXPERIMENTAL METHODS

3.1 Plasmon-resonant nanorods preparation and optical characterization

The nanorods were synthesized using previously reported seed-mediated surfactant method [11], with excess surfactant being removed by washing with chloroform. The nanorods have nominal dimensions of 15×45 nm, and in aqueous solution exhibited a peak extinction coefficient of 36 cm^{-1} at 755 nm and full-width at half maximum of 135 nm.

3.2 The spectral-domain OCT system

The spectral-domain OCT system has been described previously [10]. Briefly, a Ti:sapphire laser coupled into a single-mode fiber interferometer provided 10 mW of power at the sample with a center wavelength of 840 nm and bandwidth of 120 nm. Using a 40 mm focal length achromatic imaging lens this provided 3 μm × 16 μm resolution (axial by lateral). A computer-controlled stage laterally translated the sample while successive depth scans were acquired at 7.5 kHz by angularly dispersing the signal light onto a line camera (Dalsa Piranha 2). Calibration of the spectroscopic response of the OCT system was performed by imaging a Lambertian surface (SphereOptics, Inc.) while placing various IR filters in the sample arm beam path, as in [10].

3.3 Spectroscopic OCT in tissue phantoms

Optical tissue phantoms consisted of 2% aqueous intralipid solution and either a 0%, 20%, or 50% concentration of nanorods relative to the stock nanorod solution used for optical calibration (36 cm^{-1} peak). Images were sampled with 900 × 1024 pixels over a physical distance of 3 mm × 1.5 mm (lateral by axial). The OCT images were processed using each of the 6 methods described above, where the voxel size used for processing was 67 μm × 59 μm. The *a priori* database was determined from the control intralipid solution by collecting spectra with common depths a (within 59 μm windows) and common top surface positions z_s (8.8 μm windows). The resulting image-averaged values of ρ_n for methods 2 and 3 are reported in Table 1. For 2D image display, the OCT data channels were logarithmically scaled, and the $\mu_{t,n}$ or ρ_n data channels were scaled linearly, 2D Gaussian filtered with a $1/e$ size of 33 μm × 29 μm, and assigned to color channels in HSV or RGB color maps as described above. The results are displayed in Figure 1. Because the spectroscopic analysis near the top surface was excessively noisy due to specular reflections, voxels closer than 44 μm from the top surface z_s were removed from the analysis. Also, for regions of the samples where z_s was outside the range of values provided by the *a priori*, no $\mu_{t,n}$ or ρ_n values could be computed, and so these regions appear as blank columnar stripes at the edges of some of the images.

3.4 Human tissue imaging

A sample of human breast invasive ductal carcinoma was obtained using informed signed consent under protocols approved by the Institutional Review Boards of Carle Foundation Hospital and the University of Illinois at Urbana-Champaign. The tumor sample (~1 cm^3) was formalin-fixed and divided into two parts. Using the same sampling as for the tissue phantoms described above, each tumor portion was imaged in several locations in the *y* dimension (*N*=5 for each) to build an *a priori* database of the tumor endogenous optical response. Subsequently, one of the parts was injected with the nanorods stock solution and imaged in 8 locations by stepping 125 μm increments in *y*. Processing using methods 2 and 3 was carried out using the same technique outlined for the tissue phantoms above, except that excessively steep tumor surfaces (such as near the injection site) were excluded from the computation. The resulting image-averaged values of ρ_n for the control and nanorod-injected groups are reported in Table 2. The resulting spectroscopic 2D images using method 2.B are displayed in Figure 2.

4. RESULTS AND DISCUSSION

4.1 Spectroscopic OCT in tissue phantoms

We expect that a good processing method for the SOCT data will show a clear relationship between nanorod concentration and contrast signal for the tissue phantoms. Looking at Table 1 we see that Method 2.A is reasonably predicts the actual nanorod relative concentrations of 0, 0.2, and 0.5 for the respective tissue phantoms. However, the other methods either exhibit a negative bias and/or less increase in the measured ρ_n as the nanorod concentration is increased. Figure 1 displays the spatially resolved 2D images from each of the 6 methods. Method 1.A does

indeed show a blue-shifted wavelength centroid and increasing intensity of the residual extinction spectrum $\mu_{t,n}(\lambda)$ for increased nanorod concentration, as expected, because the nanorods extinction peak at 755 nm is well on the blue-side of the OCT imaging light centered at 840 nm. The depth-resolving method 1.B also shows some of this effect, but with greater noise at increasing depths in the intralipid. Similarly, methods 2.A and 2.B show the expected correlation between in the estimated nanorod concentration ρ_n and the actual concentration, with the depth-resolving method 2.B exhibiting more noise at greater depths. Both methods 3 are completely dominated by noise that is larger than the signal we are trying to sense (noise in ρ_n greater than 1, the stock solution concentration).

Table 1. Image-averaged measurements of the nanorod relative concentration ρ_n for 2% intralipid tissue phantoms with added nanorods by 4 of the methods described in Section 2.

Tissue Phantom	Processing Method			
	2.A	2.B	3.A	3.B
Control	0.05	0.08	-0.13	-0.005
20% Nanorods	0.11	0.07	-0.04	0.17
50% Nanorods	0.46	0.13	0.15	0.18
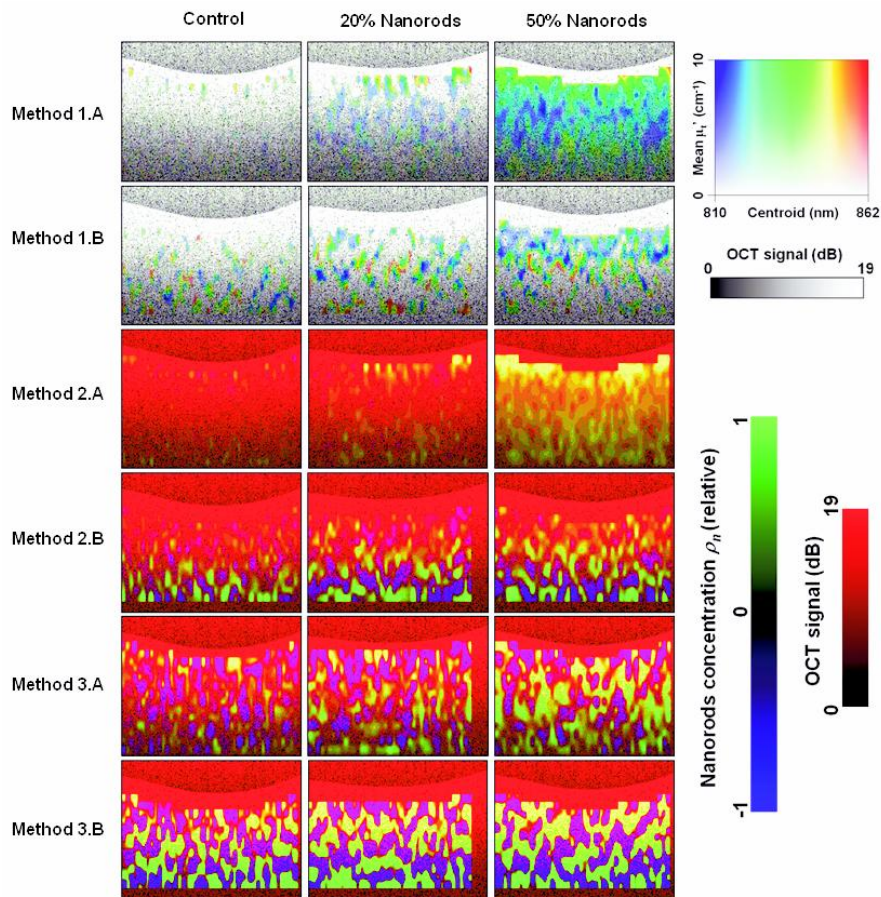
Fig. 1. Nanorod-contrasted OCT imaging of 2% intralipid tissue phantoms. Each column represents a single OCT image of a phantom containing either no nanorods, 20%, or 50% nanorods (left to right). Each row represents the results of processing by the various methods described in Section 2. The scale box and scalebar showing the HSV color mapping for Methods 1.A and 1.B are shown in the upper right. The scalebars for the RGB color mapping used in Methods 2 and 3 are shown in the lower right. Image physical dimensions are 3mm × 1mm lateral by axial.

4.2 Human tissue imaging

Ideally we expect the nanorod-injected tissues to reveal ρ_n values significantly larger than the control tissues. Looking at Table 2, we see that method 2.A reveals the opposite effect than expected: the nanorod-injected ρ_n values average to zero, whereas the control values are significantly above zero. This is surprising as method 2.A accurately predicted ρ_n for the tissue phantoms. There may be several factors which contribute to these problems. Because the tissue phantoms are liquid, Brownian motion of the scatterers may tend to broaden the spectrum of the detected backscattered light by Doppler shifting. This effect would be of much smaller magnitude in the essentially solid-phase tissues, thus, the various methods may work better or worse in the liquid or solid phase. Another undesired effect may be due to hydration of the tissues by the injection solution, which may swell the tissue and reduce its endogenous extinction. This might tend to result in a negative residual extinction measured for the nanorod-injected tissues. It is also surprising that method 2.A results in a large positive value for ρ_n for the control tissues, because they were computed based on their own images being the *a priori*. Thus, method 2.A has an inherent positive bias that needs to be resolved. Finally, a coverslip was used atop the human tissues while there was no coverslip for the phantoms.

Table 1. Image-averaged measurements of the nanorod relative concentration ρ_n for control and nanorod-injected tumors by 4 of the methods described in Section 2. Error bars are the standard deviation of the $\rho_{n,i}$ values within each group.

Tumor sample	Processing Method			
	2.A	2.B	3.A	3.B
Control	0.26 ± 0.12	0.09 ± 0.06	-0.11 ± 0.13	0.09 ± 0.07
Nanorod-Injected	-0.06 ± 0.23	0.31 ± 0.16	0.02 ± 0.14	-0.15 ± 0.11

Despite these difficulties, it appears that method 2.B may be providing nanorod-based contrast for the tumor samples, because the ρ_n of the injected samples are more than one standard deviation above the control. We displayed the 2D images resulting from this method in Fig. 2. In these images appears the bottom surface of the coverslips which were placed atop the samples and tilted from normal to avoid strong backreflection. While there is some apparent noise in these images, the nanorod-injected image set exhibits some high intensity ρ_n regions for cross-sectional slices immediately adjacent to the suspected injection site, in comparison to the control image set.

5. CONCLUSIONS

The results of producing nanorod-specific contrast in human tumors are promising, as the predicted concentration values from the nanorod-injected samples were more than one standard deviation from the controls. We proposed several methods which treat the spatial inhomogeneity of the sample in different ways. All of our methods assume the inhomogeneity is spectrally-independent, as this is the essence of being able to detect spectrally-dependent nanorods against the tissue background. These methods involve computing the residual extinction spectrum by subtracting the extinction spectrum of an *a priori* image set. The best method was method 2.B, which then fits the partial derivative with respect to z of the residual extinction spectrum with the *a priori* nanorod extinction spectrum, to estimate the depth-resolved nanorod concentration. Method 2.B assumes that the spatial inhomogeneity becomes negligible with sufficient spatial averaging (sufficiently large voxel). Thus, a depth-resolved image of the distribution of the nanorods may be constructed. However, future work is needed indeed to verify that method 2.B works in a calibrated setting, perhaps with the use of solid-phase tissue phantoms, since the results from liquid-phase phantoms did not correlate well with the actual nanorod concentration. Also, further development of other methods similar to method 3.B might be more robust to samples with spatial inhomogeneities that occur over larger areas (in other words, they do not become negligible with spatial averaging).

Eventually we hope these methods will be useful toward targeted imaging of tumors against a normal tissue background for diagnostic procedures or for surgical guidance. Currently nanorods have been conjugated with cell

surface-receptors specific to breast cancer, demonstrating cancer cell specific binding *in vitro* [12]. Hyperthermic therapy is then provided using higher laser intensities than those used in imaging, which induces cell death by compromising the cell membrane integrity [12]. Clearly, the combination of both imaging and therapy may make nanorods a useful tool for cancer diagnosis and treatment.
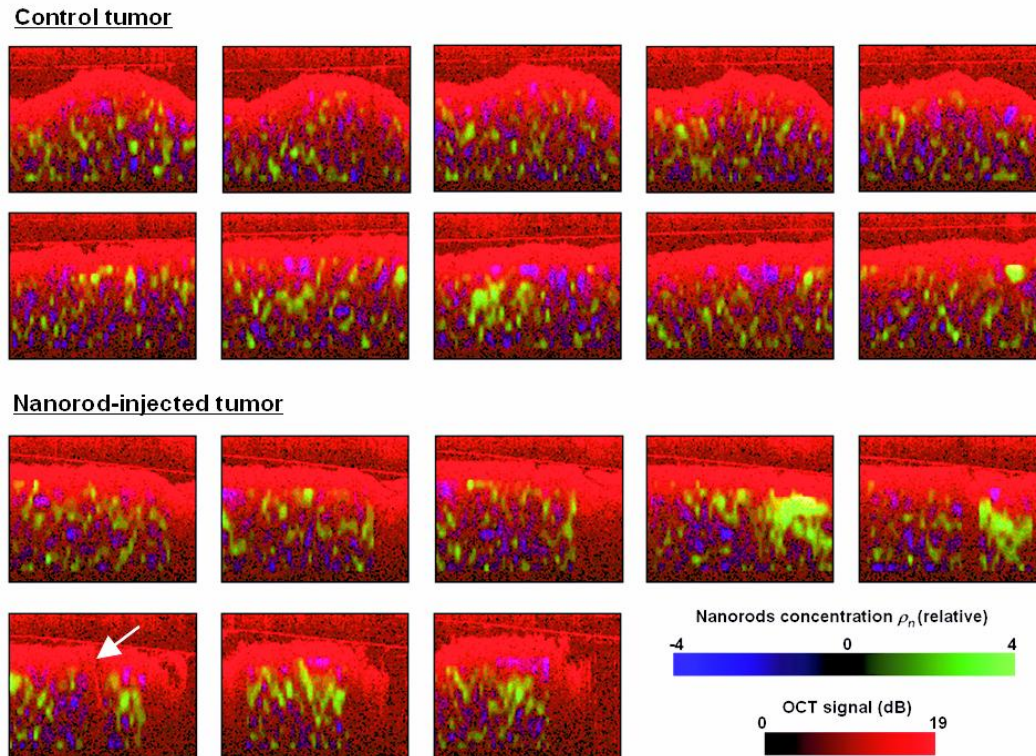
Fig. 2. Spectroscopic OCT images of human breast tumor sample without (top 10 control images) and with (bottom 8 images) injected nanorods, processed using method 2.B which spatially maps the depth-resolved nanorod concentration according to Eq. (11). The position of the suspected injection site is indicated by the arrow. Scalebars in the lower right indicate the color mapping used. Image physical dimensions are 3mm × 1mm lateral by axial.

ACKNOWLEDGEMENTS

REFERENCES

[1]   D. Huang, E. A. Swanson, C. P. Lin, J. S. Schuman, W. G. Stinson, W. Chang, M. R. Hee, T. Flotte, K. Gregory, C. A. Puliafito, and J. G. Fujimoto, "Optical coherence tomography," Science, **254(5035)**, 1178-1191 (1991).

[2]   B. E. Applegate and J. A. Izatt, "Molecular imaging of endogenous and exogenous chromophores using ground state recovery pump-probe optical coherence tomography," Opt. Express **14(20)**, 9142-9155 (2006).

[3]   A. L. Oldenburg, F. J.-J. Toublan, K. S. Suslick, A. Wei, and S. A. Boppart, "Magnetomotive contrast for *in vivo* optical coherence tomography," Opt. Express **13(17)**, 6597-6614 (2005).

[4]   A. Agrawal, S. Huang, A. W. H. Lin, M.-H. Lee, J. K. Barton, R. A. Drezek, and T. J. Pfefer, "Qualitative evaluation of optical coherence tomography signal enhancement with gold nanoshells," J. Biomed Opt. **11(4)**, 041121 (2006).

[5]   H. Cang, T. Sun, and Z.-Y. Li, "Gold nanocages as contrast agnets for spectroscopic optical coherence tomography," Opt. Lett. **30(22)**, 3048-3050 (2005).

[6]   A. L. Oldenburg, M. N. Hansen, D. A. Zweifel, A. Wei, and S. A. Boppart, "Plasmon-resonant gold nanorods as low backscattering albedo contrast agents for optical coherence tomography," Opt. Express **14(15)**, 6724-6738 (2006).

[7]   U. Morgner, W. Drexler, F. C. Kartner, X. D. Li, C. Pitris, E. P. Ippen, and J. G. Fujimoto, "Spectroscopic optical coherence tomography," Opt. Lett. **25(2)**, 111-113 (2000).

[8]   C. Xu, J. Ye, D. L. Marks, and S. A. Boppart, "Near-infrared dyes as contrast-enhancing agents for spectroscopic optical coherence tomography," Opt. Lett. **29(14)**, 1647-1649 (2004).

[9]   C. Xu, D. L. Marks, M. N. Do, and S. A. Boppart, "Separation of absorption and scattering profiles in spectroscopic optical coherence tomography using a least-squares algorithm," Opt. Express **12(2)**, 4790-4803 (2004).

[10]   A. L. Oldenburg, C. Xu, and S. A. Boppart, "Spectroscopic optical coherence tomography and microscopy," IEEE J. Sel. Top. Quan. Elec., **13(6)**, in press (2007).

[11]   D. A. Zweifel and A. Wei, "Sulfide-arrested growth of gold nanorods," Chem. Mater. **17(16)**, 4256-4261 (2005).

[12]   L. Tong, Y. Zhao, T. B. Huff, M. H. Hansen, A. Wei, and J.-X. Cheng, "Gold nanorods mediate tumor cell death by compromising membrane integrity," Adv. Mater. **19**, 3136-3141 (2007).